NEUROSCIENCE

A genetically encoded far-red fluorescent indicator for imaging synaptically released Zn^{2+}

Tianchen Wu[1]†, Manoj Kumar[2]†, Jing Zhang[1], Shengyu Zhao[1,3], Mikhail Drobizhev[4], Mason McCollum[5], Charles T. Anderson[5], Ying Wang[6], Antje Pokorny[6], Xiaodong Tian[1], Yiyu Zhang[1], Thanos Tzounopoulos[2]*, Hui-wang Ai[1,3,7]*

Synaptic zinc ion (Zn^{2+}) has emerged as a key neuromodulator in the brain. However, the lack of research tools for directly tracking synaptic Zn^{2+} in the brain of awake animals hinders our rigorous understanding of the physiological and pathological roles of synaptic Zn^{2+}. In this study, we developed a genetically encoded far-red fluorescent indicator for monitoring synaptic Zn^{2+} dynamics in the nervous system. Our engineered far-red fluorescent indicator for synaptic Zn^{2+} (FRISZ) displayed a substantial Zn^{2+}-specific turn-on response and low-micromolar affinity. We genetically anchored FRISZ to the mammalian extracellular membrane via a transmembrane (TM) α helix and characterized the resultant FRISZ-TM construct at the mammalian cell surface. We used FRISZ-TM to image synaptic Zn^{2+} in the auditory cortex in acute brain slices and awake mice in response to electric and sound stimuli, respectively. Thus, this study establishes a technology for studying the roles of synaptic Zn^{2+} in the nervous system.

INTRODUCTION

The existence of free or labile zinc ions (Zn^{2+}) and Zn^{2+}-containing vesicles in the brain has been known for decades (*1*–*3*). Recent studies have established the role of synaptically released Zn^{2+} in modulating neurotransmission (*4*–*12*). A substantial subset of neurons accumulates Zn^{2+} in synaptic vesicles via the vesicular Zn^{2+} transporter (ZnT3) and release Zn^{2+} in an activity-dependent manner (*4*, *13*, *14*). Synaptically released Zn^{2+} modulates the activity of glutamate receptors, such as *N*-methyl-D-aspartate receptors (NMDARs) (*4*, *9*, *12*), α-amino-3-hydroxy-5-methyl-4-isoxazole-propionic acid receptors (AMPARs) (*5*), and kainate receptors (*15*–*17*); γ-aminobutyric acid (GABA) receptors (*11*, *18*–*20*); and glycine receptors (*21*, *22*). In addition, synaptic Zn^{2+} may enter postsynaptic neurons via voltage-gated Ca^{2+} channels or Ca^{2+}-permeable AMPARs to trigger intracellular signaling cascades (*3*, *23*). Dysregulation of synaptic Zn^{2+} signaling has been linked to numerous neurological diseases, such as stroke, epilepsy, depression, Alzheimer's disease, and hearing disorders (*24*–*26*).

Although the importance of Zn^{2+} in the nervous system has been widely accepted, a detailed mechanistic understanding of Zn^{2+}-dependent neuromodulation is still missing. Current studies on Zn^{2+} signaling in the brain often rely on Ca^{2+} indicators (e.g., GCaMPs) (*27*) to monitor neuronal activities in response to perturbations with Zn^{2+} chelators (e.g., ZX1) (*4*, *28*) or genetic elimination of vesicular (synaptic) Zn^{2+} using ZnT3 knockout (KO) mouse (*14*). These approaches can neither distinguish direct versus circuit-dependent synaptic Zn^{2+} effects nor assess Zn^{2+} dynamics during neuromodulation. A further understanding of the physiological and pathological roles of synaptic Zn^{2+} in the nervous system requires convenient and robust tools to track synaptic Zn^{2+} dynamics directly in the brain in behaving animals during normal and pathological conditions.

Traditionally, biological Zn^{2+} has been studied with histochemical procedures, such as dithizone-based colorimetric staining and Timm's staining (*1*, *29*). These invasive methods cannot be applied to living organisms and only provide an endpoint snapshot on Zn^{2+} localization. Over the past several decades, researchers have developed a number of fluorescent Zn^{2+} indicators, including small-molecule sensors, genetically encoded sensors, and hybrid sensors (*30*, *31*). Although synthetic and hybrid Zn^{2+} indicators have proven to be invaluable tools, it is challenging to use them for repeated measurements in live animals. In addition, it is difficult to maintain a stable concentration of exogenously loaded fluorescent indicators for detecting secreted Zn^{2+} in the extracellular space in living organisms. Alternatively, genetically encoded fluorescent indicators have shown promising results and gained much interest. They often display high specificity and are compatible with signal peptides for convenient subcellular localization. Moreover, they can be readily delivered into live cells and organisms to achieve transient or long-term expression (*32*, *33*). Furthermore, genetically encoded indicators are compatible with various viral vectors and genetically modified animals, allowing studies concerning specific cell types or brain regions. Last, plasmids and viral vectors encoding genetically encoded indicators can be broadly disseminated and readily adopted by other interested researchers.

Seminal works by Merkx, Palmer, and their co-workers have led to a family of genetically encoded Zn^{2+} indicators (GEZIs) mainly based on the Zn^{2+}-dependent modulation of Förster resonance energy transfer (FRET) between two fluorescent proteins (FPs) (*31*, *32*, *34*, *35*). These ratiometric GEZIs have become powerful

[1]Department of Molecular Physiology and Biological Physics, and Center for Membrane and Cell Physiology, University of Virginia School of Medicine, Charlottesville, VA 22908, USA. [2]Department of Otolaryngology, Pittsburgh Hearing Research Center, University of Pittsburgh, Pittsburgh, PA 15261, USA. [3]Department of Chemistry, University of Virginia, Charlottesville, VA 22904, USA. [4]Department of Microbiology and Cell Biology, Montana State University, Bozeman, MT 59717-384, USA. [5]Department of Neuroscience, Rockefeller Neuroscience Institute, West Virginia University School of Medicine, Morgantown, WV 26506, USA. [6]Department of Chemistry and Biochemistry, University of North Carolina Wilmington, Wilmington, NC 28403, USA. [7]The UVA Comprehensive Cancer Center, University of Virginia, Charlottesville, VA 22908, USA.
*Corresponding author. Email: huiwang.ai@virginia.edu (H.-w.A.); thanos@pitt.edu (T.T.)
†These authors contributed equally to this work.

tools for imaging Zn^{2+} in intracellular space and organelles (*34*, *35*). However, they have relatively large molecular sizes and broad fluorescence excitation and emission profiles, making it challenging to perform multicolor or/and multiplexed experiments. Furthermore, their modest dynamic range represents a hurdle for in vivo imaging applications. Thus, recent efforts by us and others have developed single-FP–based, green fluorescent intensiometric GEZIs (*36*–*39*). Despite the progress, fluorescence imaging of synaptic Zn^{2+} release in the brain in awake animals has not yet been achieved because of several remaining technical hurdles. First, previous GEZIs were typically optimized for imaging intracellular free Zn^{2+}, and their affinities are too high for monitoring extracellular synaptically released Zn^{2+} (*32*, *40*). Moreover, most GEZIs cannot be effectively routed to the exoplasmic membrane (*36*). Given that synaptic Zn^{2+} is organized into distinct spatial microdomains around the plasma membrane to modulate neurotransmission (*12*), the lack of extracellular membrane–bound sensors has been a major obstacle to tracking synaptic Zn^{2+} dynamics in vivo.

The two exceptions are our previously developed ZnGreen2 and ZIBG2, which have high-nanomolar to low-micromolar affinities suited for detecting Zn^{2+} secretion from intracellular vesicles (*36*, *37*). In addition, they use *Pyrococcus furiosus* Rad50 (*pf*Rad50) zinc hook peptides as the sensory elements, allowing a more effective localization of the GEZIs to the extracellular surface of mammalian cells via a platelet-derived growth factor receptor (PDGFR) transmembrane (TM) α helix (*36*, *37*). However, ZnGreen2 bestowed very poor photostability due to a reversible photoswitching of the chromophore, a phenomenon previously observed in photoswitchable FPs (*41*). Because ZnGreen2 is a Zn^{2+}-dependent fluorescence turn-off indicator, the photoswitching phenomenon made the interpretation of results unreliable. On the other hand, ZIBG2 has much-enhanced photostability, but its small dynamic range precludes its usefulness in vivo (*36*). Therefore, our previous attempts to use extracellular membrane–bound ZnGreen2 or ZIBG2 to image synaptic Zn^{2+} secretion in the brain in mice were unsuccessful.

To address the limitations, we here engineered a far-red fluorescent indicator for synaptic Zn^{2+} (FRISZ). We genetically anchored FRISZ to the extracellular membrane and validated the indicator for imaging synaptic Zn^{2+} release in acute brain slices and awake mice in response to electric or sound stimuli.

RESULTS

Engineering of an FRISZ

Our previous studies grafted the *pf*Rad50 zinc hook sensory elements to the two termini of circularly permuted green FPs (GFPs) (*36*, *37*). In the resultant indicators, Zn^{2+} binding was expected to induce zinc hook homodimerization (*42*), leading to Zn^{2+}-dependent fluorescence changes. We recently converted a far-red FP, mMaroon1 (*43*), into several bright, circularly permuted (cpmMaroon) variants with excitation and emission maxima above 600 nm (*44*). Built upon these results, we examined the fusion of *pf*Rad50 zinc hook peptides to our recent cpmMaroon variants.

To date, single FP–derived indicators are almost always based on circularly permuted FPs (cpFPs) with termini in β strand 7, and the modulation of chromophore ionization by the fused sensory domains is considered crucial for the responsiveness of these indicators (*33*). However, we were unable to generate fluorescent cpmMaroon variants with circular permutation sites in β strand 7 of mMaroon1 (*44*). Fortunately, we identified two cpmMaroon variants, namely, cpmMaroon185-186 and cpmMaroon196-186, with circular permutation sites in the loop between β strands 9 and 10 but still sensitive to pH changes around pH 7.4 (fig. S1) (*44*). We genetically fused a copy of the zinc hook to each of the termini of cpmMaroon185-186 or cpmMaroon196-186. Grafting the zinc hooks to cpmMaroon185-186 resulted in a fusion protein showing a 40% fluorescence increase upon Zn^{2+} addition (Fig. 1 and fig. S2). To improve fluorescence responsiveness, we next randomized the two linkers between cpmMaroon185-186 and the zinc hook elements using overlap polymerase chain reactions (PCRs) based on synthetic oligonucleotides with degenerate codons at desired sites. Screening of these libraries led to a twofold increase in Zn^{2+}-dependent

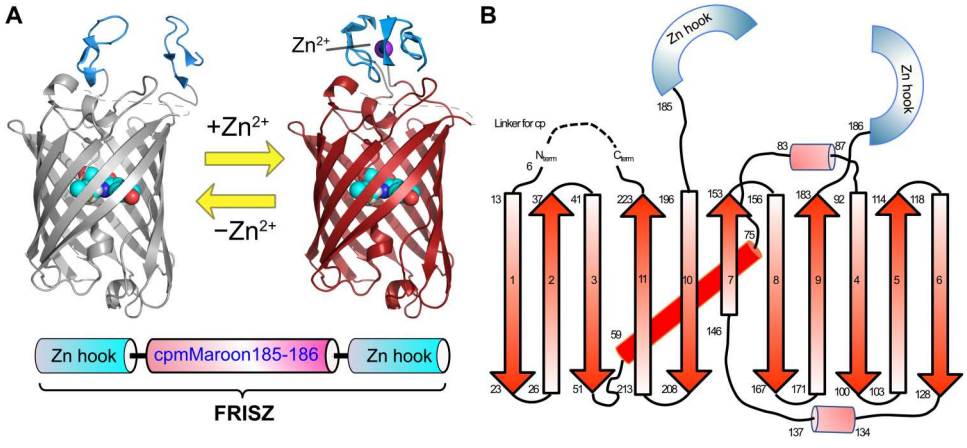

Fig. 1. Illustration of the Zn^{2+}-sensing mechanism and the secondary structure of FRISZ. (**A**) Illustration of FRISZ, in which two Rad50 zinc hook motifs are fused to the N and C termini of cpMaroon185-186. The domain arrangement of the primary sequence is also presented at the bottom. (**B**) Schematic representation of the secondary structure elements of FRISZ. Secondary structure elements in cpmMaroon185-186 are based on a mMaroon1 structure predicted by SWISS-MODEL using mCardinal (Protein Data Bank: 4OQW) as the template. Cylinders represent α helices, and arrows represent β strands. The Rad50-derived zinc hook motifs are presented as blue semicircles.

fluorescence response. Moreover, we carried out random mutagenesis using error-prone PCRs and performed 11 rounds of directed evolution (figs. S2 and S3), further enhancing the indicator's Zn^{2+} responsiveness by approximately eightfold. Last, because we aim to target the indicator to the extracellular surface, which is a relatively oxidizing environment compared to the cytosol, we examined whether the Cys residues in the zinc hook elements could be replaced with His. His can coordinate with Zn^{2+}, but it is more resistant to oxidation than Cys. Previously, His has been used to replace Cys to derive artificial His^4 zinc fingers (*45*). In addition, another study successfully replaced Zn^{2+}-binding Cys residues in an FRET-based GEZI to derive a His^4 indicator with a reduced redox sensitivity (*35*). We, therefore, mutated the four Cys residues in our indicator to His, and we found that the replacement had a very minimal impact on the indicator's dynamic range (figs. S2 and S3). We named the final variant "FRISZ," a fusion of Cys-free *pf*Rad50 zinc hook peptides and cpmMaroon185-186, which was optimized through the multistep protein engineering process.

Spectroscopic and biophysical characterization

To quantitatively determine the spectroscopic and biophysical properties of FRISZ, we prepared the purified protein from *Escherichia coli*. FRISZ exhibited a Zn^{2+}-dependent ~7-fold (F/F_0) fluorescence turn-on response (Fig. 2A). Its one-photon fluorescence excitation and emission maxima were ~607 and 650 nm, respectively. When adding Zn^{2+} to the protein, we observed an increase in the absorption at ~607 nm and a simultaneous absorption decrease at ~460 nm (Fig. 2B), suggesting a Zn^{2+}-dependent chromophore deprotonation process. Next, we quantified the fluorescence quantum yield of the protein in the Zn^{2+}-free and Zn^{2+}-bound states, and the Zn^{2+} addition enhanced the quantum yield by ~2-fold (Table 1). Thus, both chromophore ionization and fluorescence quantum yield changes are responsible for the substantial turn-on response of FRISZ. Moreover, we measured fluorescence lifetimes using a frequency-domain method (fig. S4). The average fluorescence lifetimes for FRISZ in the Zn^{2+}-free and Zn^{2+}-bound states were ~0.51 and 0.83 ns, respectively (Table 1). Furthermore, we determined extinction coefficients based on gradual alkaline titrations (fig. S5) and the Strickler-Berg formula (*46*). In the Zn^{2+}-bound state, the molecular brightness of FRISZ was ~50% of mMaroon1 (Table 1). We further measured the fluorescence of FRISZ in the presence of various concentrations of Zn^{2+}, and the apparent dissociation constant from the steady-state measurement ($K_{d,steady}$) was determined to be ~8.8 μM (Fig. 1C). We also performed kinetic measurement using a stopped-flow fluorescence spectrophotometer and obtained association and dissociation rate constants ($k_{on} = 0.49 \pm 0.01\ s^{-1}\ \mu M^{-1}$, $k_{off} = 3.5 \pm 0.3\ s^{-1}$) (fig. S6). Therefore, the dissociation constant from the kinetic measurement ($K_{d,kinetic}$) was determined to be ~7.1 μM, which is quite close to the number from the steady-state measurement. In addition, we examined the specificity of FRISZ. Except for Zn^{2+}, other tested biologically relevant metal ions induced no or minimal fluorescence changes (Fig. 1D). Under two-photon excitation conditions, FRISZ displayed excitation peaks at 1128 and 1216 nm (Fig. 2E). Superior two-photon brightness and Zn^{2+}-induced fluorescence responses were obtained between 1050 and 1250 nm (Table 1 and Fig. 2F). Together, these results suggest that FRISZ is a high-quality fluorescent Zn^{2+} indicator under both one-photon and two-photon excitation conditions.

Characterization of FRISZ at the mammalian cell surface

To anchor FRISZ to the extracellular membrane, we inserted the gene into the commercial pDisplay plasmid, which encodes an N-terminal cleavable immunoglobin κ (Igκ) leader sequence for mammalian secretory pathway targeting and a C-terminal PDGFR TM domain for cell surface anchoring (Fig. 3A). We observed cytoplasmic membrane localization of FRISZ in transiently transfected

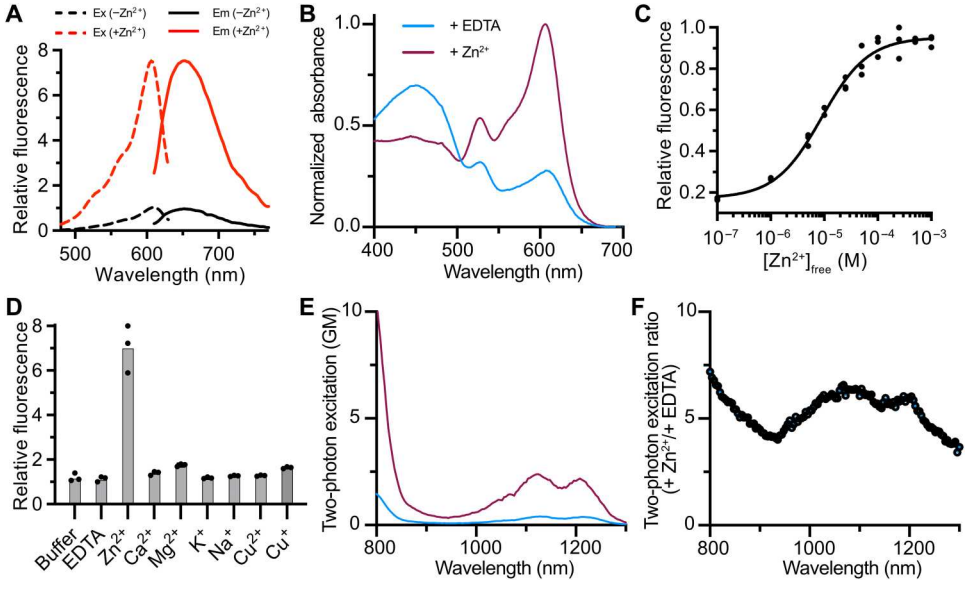

Fig. 2. Spectroscopic characterization of FRISZ as a purified protein. (**A**) Excitation (dashed line) and emission (solid line) spectra of purified FRISZ in the presence of 100 μM Zn^{2+} (red) or 100 μM EDTA (black). (**B**) One-photon absorbance spectra of FRISZ in the presence of 100 μM Zn^{2+} or 100 μM EDTA. (**C**) Dose-response curve of purified FRISZ (K_d = 8.8 ± 1.0 μM), n = 3. (**D**) Fluorescence of FRISZ in response to Zn^{2+} and other indicated chemicals (100 μM), n = 3. (**E**) Two-photon fluorescence excitation spectra of FRISZ in the presence of 100 μM Zn^{2+} or 100 μM EDTA. (**F**) The ratio of two-photon excitation plotted against wavelength.

Table 1. Photophysical properties of FRISZ and other related proteins. N/A, not applicable; N/D, not determined.

Protein name	FRISZ		mMaroon1*	cpmMaroon185-186†
	Zn^{2+}-free	Zn^{2+}-bound		
Peak excitation λ_{ex} (nm)	607	606	609	610
Peak emission λ_{em} (nm)	650	654	657	648
F/F_0	7.04 ± 1.06		N/A	N/A
$K_{d,\ steady}$ (μM)	8.77 ± 0.99		N/A	N/A
Apparent Hill coefficient (n_H)	0.94 ± 0.10		N/A	N/A
$K_{d,\ kinetics}$ (μM)	7.14 ± 0.55		N/A	N/A
Fluorescence lifetime τ (ns)	0.51 ± 0.03	0.83 ± 0.05	N/D	N/D
Relative fraction of "anionic" chromophore ρ_A	0.19 ± 0.02	0.49 ± 0.05	N/D	N/D
Effective extinction coefficient ε (mM^{-1} cm^{-1})‡	11.5 ± 1.4	32 ± 4	80	54
Quantum yield ϕ	0.075 ± 0.003	0.14 ± 0.01	0.11	0.11
One-photon brightness (ε × ϕ)	0.86 ± 0.10	4.5 ± 0.5	8.8	5.9
Two-photon brightness (GM) at the indicated excitation wavelength	0.41 ± 0.07 (1128 nm)	2.4 ± 0.4 (1124 nm)	N/D	N/D
	0.38 ± 0.07 (1216 nm)	2.2 ± 0.4 (1208 nm)		
F/F_0 at indicated two-photon excitation wavelength	6.5 ± 0.6 (1064 nm)		N/A	N/A
	6.1 ± 0.5 (1124 nm)			
	5.9 ± 0.5 (1208 nm)			

*Values adapted from (*43*). †Values adapted from (*44*). ‡Presented as per millimolars of the total protein (a product of ρ_A and the true extinction coefficient per millimolars of the anionic chromophore).

human embryonic kidney (HEK) 293 T cells (Fig. 3A and fig. S7). Furthermore, Zn^{2+} addition triggered a robust fluorescence increase (F/F_0 = ~3) of cell surface–localized FRISZ (FRISZ-TM) (Fig. 3, A and B). In contrast, we consistently observed no fluorescence response from cell surface–localized mMaroon1 (mMaroon1-TM, Zn^{2+}-nonresponsive negative control). The fluorescence increase of FRISZ-TM was dependent on Zn^{2+} concentrations, and the dissociation constant at the cell surface was determined to be ~7.3 μM (Fig. 3, B and C). Moreover, we imaged the HEK 293 T cells while locally applying Zn^{2+} via a micropipette. We determined the half-time ($t_{0.5}$) for fluorescence rise (Zn^{2+} association) and decay (spontaneous dissociation) to be 117 ms and 1.28 s, respectively (Fig. 3D). In addition, we compared the photostability of cell surface–localized FRISZ with mMaroon1 and the commonly used superfolder GFP (sfGFP) (*43*, *47*). Under our experimental condition (continuous wide-field illumination of ~1.35 W/cm^2), FRISZ was more photostable than mMaroon1 and sfGFP (fig. S8). Thus, the results collectively suggest that FRISZ-TM is promising for monitoring the dynamics of vesicular zinc release.

FRISZ-TM detects synaptic Zn^{2+} in acute brain slices

To test the ability of FRISZ-TM to track synaptic Zn^{2+}, we used an ex vivo paradigm. ZnT3, the vesicular zinc transporter, is strongly expressed in the neocortex, including the auditory cortex (AC) (*2*, *16*). During the past few years, our studies established that cortical synaptic Zn^{2+} signaling is elicited by sound stimuli and modulates the sound frequency selectivity of the primary AC (A1) neurons in a cell-specific manner; this modulation is associated with improved sound frequency discrimination (*48*, *49*). Moreover, cortical synaptic Zn^{2+} signaling is necessary for cortical adaptation to changes in background sound stimulus statistics (*50*). Therefore, to test the feasibility of FRISZ-TM in detecting stimulus-dependent synaptic Zn^{2+} release, we performed ex vivo imaging of FRISZ-TM in acute brain slices containing the AC. To express FRISZ-TM in neurons, we prepared an adeno-associated virus (AAV) with a human synapsin 1 (hSyn) promoter (Fig. 4A). Next, we administered the FRISZ-TM AAV into the AC of C57BL/6J mice, and 3 to 4 weeks after viral injection, we prepared acute brain slices containing the AC. As described previously (*51*), we identified the AC based on anatomical landmarks, such as the rhinal fissure and the underlying hippocampal formation (Fig. 4B). We detected bright far-red fluorescence at this region of the slices, verifying the expression of FRISZ-TM or mMaroon1-TM (Fig. 4B). To image stimulus-dependent synaptic Zn^{2+} release, we positioned a stimulating electrode around layer 4 (L4) and delivered electric pulses at 100 Hz as described previously (*5*). We imaged FRISZ-TM signals from a 100 μm–by–50 μm–wide region of interest (ROI) in AC L2/3 (Fig. 4, B and C). We found that 10 to 100 pulses evoked robust and reproducible, stimulus intensity–dependent fluorescence increases in FRISZ-TM signals (Fig. 4, D and E, black) that were significantly reduced by the application of ZX1 (*4*, *28*), an extracellular Zn^{2+} chelator (Fig. 4, D and E, red). We did not observe any stimulus-dependent fluorescence increase in AC slices from mMaroon1-TM–expressing mice (Fig. 4, D and E, blue), and ZX1 did not have any effect on these negative controls (Fig. 4, D and E, magenta). Together, these results show that FRISZ-TM detects electrically evoked extracellular Zn^{2+} in acute brain slices.

To track the origin of extracellular Zn^{2+} detected by FRISZ-TM, we performed similar experiments in AC brain slices prepared from ZnT3 KO mice lacking synaptic Zn^{2+} (*14*). We used ZnT3-

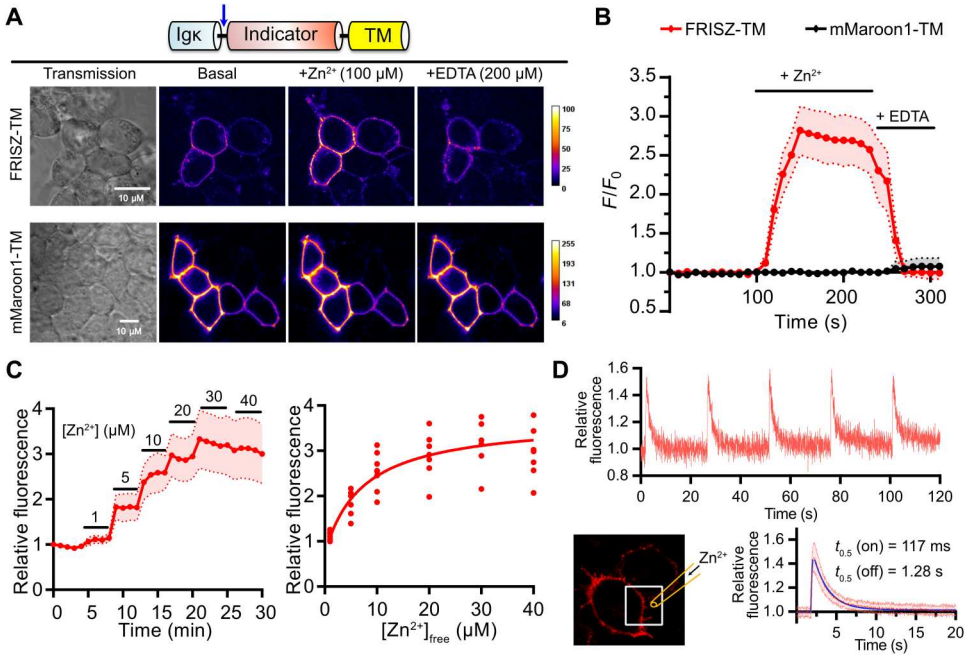

Fig. 3. Characterization of FRISZ at the mammalian cell surface. (**A**) Top: Schematics of the genetic elements for the localization of FRISZ or mMaroon1 at the mammalian cell surface. Igκ, murine Igκ chain signal peptide. TM, PDGFRβ transmembrane domain. The arrow indicates the signal peptide cleavage site. Bottom: Representative pseudo-color images of FRISZ or mMaroon1 at the surface of HEK 293 T in response to Zn^{2+} and EDTA. This experiment was repeated three times with similar results using independent cultures. Scale bars, 10 μm. (**B**) Quantification of time-lapse responses of FRISZ or mMaroon1 at the surface of HEK 293 T cells to 100 μM Zn^{2+} and 200 μM EDTA. $n = 10$ cells from three cultures. (**C**) Dose-response of FRISZ at the surface of HEK 293 T ($K_d = 7.3 \pm 3.2$ μM). Data are presented as means and SD of eight cells. (**D**) Response of FRISZ at the surface of HEK 293 T to puff application of Zn^{2+}. Top: Five sequential applications to a single cell. Bottom: Data presented as means and SD of 30 repeats (six cells with five applications each) and fitted for monoexponential growth and decay.

expressing littermates [wild type (WT)] as the control. We observed robust stimulus-dependent fluorescence increases in brain slices from ZnT3 WT mice (Fig. 4, F and G, black), and the increases were significantly reduced by ZX1 (Fig. 4, F and G, red). In ZnT3 KO mice, we observed an electrically evoked slight increase in FRISZ-TM signals that was, however, independent of either stimulus intensity (Fig. 4, F and G, cyan) or ZX1 (Fig. 4, F and G, orange). This result, in combination with the observation that ZX1 did not completely abolish the stimulus-dependent increase in FRISZ-TM fluorescence in either C57BL/6J or ZnT3 WT mice (Fig. 4, D and F, red), indicates that FRISZ-TM likely detects some nonspecific, Zn^{2+}-independent signals (see Discussion). Nonetheless, the results collectively support that FRISZ-TM responds to stimulus-evoked ZnT3-dependent synaptic Zn^{2+} signals in acute brain slices.

FRISZ-TM detects synaptic Zn^{2+} in awake mice during audition

To test whether FRISZ-TM detects synaptic Zn^{2+} signals in response to natural stimuli, we used an in vivo paradigm. Namely, we expressed FRISZ-TM in the AC neurons of C57BL/6J mice using the AAV and performed in vivo wide-field transcranial imaging in response to sound stimuli (Fig. 5, A and B). We detected bright far-red fluorescence from the A1 of mice expressing either FRISZ-TM or the mMaroon1-TM control (Fig. 5C). We next presented broadband sounds [6 to 64 kHz, 100 ms long, at 30- to 80-dB sound pressure level (SPL) in 5-dB SPL steps in random order] to the awake mice and observed robust and reproducible sound intensity–dependent increases in fluorescence in FRISZ-TM-expressing mice (Fig. 5, D and E, black). Infusion of ZX1 (*4*, *28*) into the A1 largely suppressed sound-evoked fluorescent signals, further confirming that the signal of FRISZ-TM was dependent on extracellular Zn^{2+} (Fig. 5, D and E, red). Furthermore, the mMaroon1-TM–negative control mice showed negligible response to sound stimulation in either the absence (Fig. 5, D and E, blue) or presence of ZX1 infusion (Fig. 5, D and E, magenta). These results suggest that FRISZ-TM detects sound intensity–dependent increases in A1 extracellular Zn^{2+} levels in awake mice.

To examine the origin of extracellular Zn^{2+} detected by FRISZ-TM, we performed wide-field transcranial imaging with ZnT3 WT and KO mice. We observed robust sound intensity–dependent fluorescence increases in ZnT3 WT mice (Fig. 5, F and G, black) that were significantly reduced with the infusion of ZX1 (Fig. 5, F and G, red). However, we did not observe any sound-evoked fluorescence increase in ZnT3 KO mice (Fig. 5, F and G, cyan and orange), suggesting that FRISZ-TM selectively detects sound-evoked ZnT3-dependent synaptic Zn^{2+} signals in awake mice.

DISCUSSION

We have engineered the first far-red fluorescent GEZI by genetically fusing Rad50 zinc hook elements to cpmMaroon185-186, followed by multisteps of directed evolution. FRISZ responded to low-micromolar Zn^{2+} with excellent specificity and response magnitude. We further anchored FRISZ to the cell surface and validated this tool in measuring synaptic Zn^{2+} signals in brain slices and awake mice in response to electrical and sound stimuli, respectively. Our results

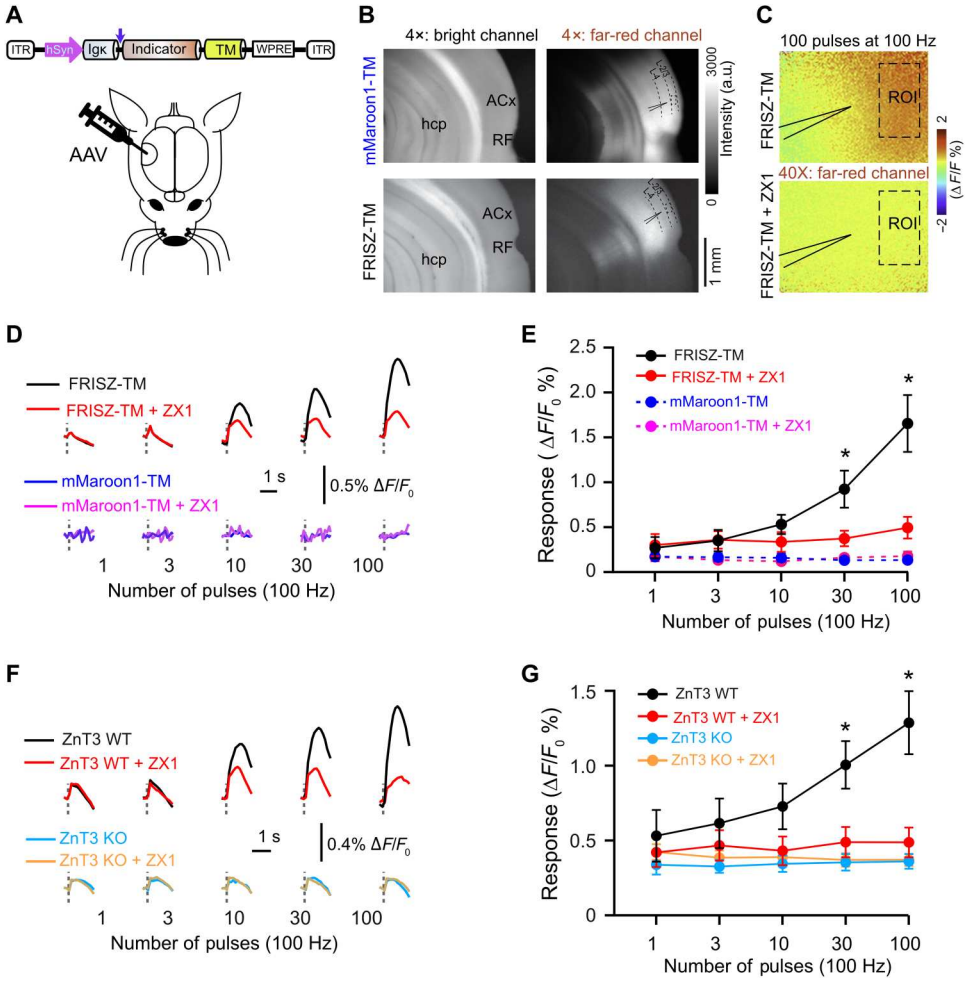

Fig. 4. Imaging of synaptic Zn^{2+} with FRISZ-TM in acute mouse brain slices. (**A**) Schematics of the genetic elements of AAVs and viral injection into mouse AC. ITR, inverted terminal repeats; WPRE, woodchuck hepatitis virus post-transcriptional regulatory element. (**B**) Left: Bright-field image of a brain slice showing the AC, the rhinal fissure (RF), and the underlying hippocampal (hcp) formation that allowed us to locate the AC. Right: Expression of mMaroon1-TM (top) and FRISZ-TM (bottom) under the far-red channel. a.u., arbitrary units. (**C**) Electrical stimulation (100 pulses at 100 Hz) of AC L4 evoked FRISZ-TM signal changes in L2/3 of AC before (top) and (bottom) after ZX1 application. (**D**) FRISZ-TM (top) or mMaroon1-TM (bottom) fluorescence signals in response to electric stimuli before (black or blue) and after (red or magenta) ZX1 infusion in C57BL/6J mice. (**E**) Summary plot of average stimulus-evoked fluorescence signals of FRISZ-TM (n = 5) and mMaroon1-TM (n = 4) mice [FRISZ-TM: control versus ZX1: two-way analysis of variance (ANOVA); effect of ZX1, F = 9.0, P = 0.03; *P < 0.05, compared to ZX1, Holm-Bonferroni's post hoc]. Dotted lines represent nonsignificant responses. (**F**) FRISZ-TM fluorescence signals in response to electric stimuli before (black or cyan) and after ZX1 infusion (red or orange) in ZnT3 WT (top) and KO (bottom) mice. (**G**) Summary plot of average stimulus-evoked fluorescence changes of FRISZ-TM in slices from ZnT3 WT (n = 5) and KO (n = 5) mice. (ZnT3 WT: control versus ZX1: two-way ANOVA; effect of ZX1, F = 44.9, $P = 2 \times 10^{-5}$; *P < 0.05, compared to ZX1, Holm-Bonferroni's post hoc). See table S1 for statistical details. Error bars indicate SEM.

collectively support that FRISZ is a useful tool for studying Zn^{2+} dynamics during synaptic stimulation and sensory processing.

We developed FRISZ from cpmMaroon185-186, which has termini between β strands 9 and 10 within the typical FP fold (Fig. 1). FRISZ thus has a different topology from other single-FP–based indicators, which typically use cpFPs with termini in β strand 7 (*33*). One previous study reported several voltage indicators derived from mKate circularly permuted between β strands 9 and 10, but the responses of those voltage indicators were mediocre (*52*). Therefore, FRISZ provides a successful example of building highly responsive FP-based indicators in this underexplored topology, and we expect our result to inspire future sensor development.

It is a long-sought-after goal to engineer genetically encoded indicators with excitation and emission in the 600- to 900-nm near-infrared (NIR) optical window. The red-shifted indicators would require lower-energy and less-damaging photons for excitation than common genetically encoded indicators based on GFPs or red FPs. Moreover, red-shifted indicators are expected to enhance imaging depth because of reduced light scattering, absorption, and autofluorescence of animal tissue (*53*). Previously, NIR Ca^{2+} indicators were developed from a biliverdin-binding NIR FP (*54*, *55*), but the requirement of the biliverdin cofactor is an obvious limitation because biliverdin is involved in normal physiology (*56*) and possibly limited under many conditions (*57*).

FRISZ belongs to an emerging class of genetically encoded far-red fluorescence indicators, which do not require biliverdin and can spontaneously form chromophores within their peptide sequences. FRISZ exhibited peak excitation and emission above 600 nm and is

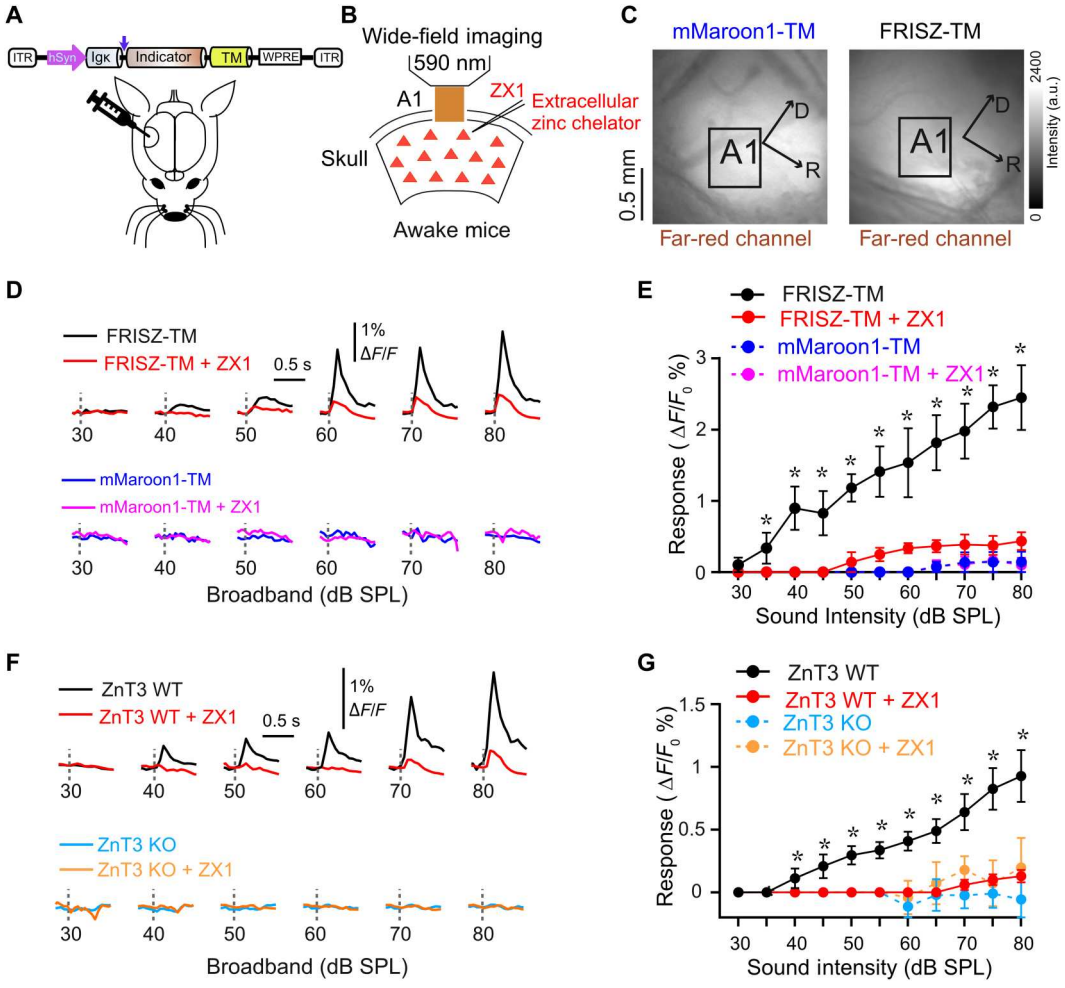

Fig. 5. Imaging of synaptic Zn^{2+} with FRISZ-TM, in response to sound stimuli in awake mice. (**A**) Schematics of AAV genetic elements and injection into mouse AC. (**B**) Illustration of transcranial imaging of FRISZ-TM or mMaroon-TM in head-fixed awake mice. ZX1 was infused into the AC via a glass pipette connected to a syringe pump. (**C**) Fluorescence images of the primary AC (A1) showing the expression of mMaroon1-TM (left) and FRISZ-TM (right). D, dorsal; R, rostral. (**D**) Representative transcranial FRISZ-TM (top) or mMaroon1-TM (bottom) fluorescence signals in response to broadband sounds before (black or blue) and after (red or magenta) ZX1 infusion in C57BL/6J mice. (**E**) Summary plot of average sound-evoked fluorescence signals of FRISZ-TM ($n = 5$) and mMaroon1-TM ($n = 3$) in C57BL/6J mice. (FRISZ-TM: control versus ZX1: two-way ANOVA; effect of ZX1, $F = 12.01$, $P = 1.0 \times 10^{-6}$; *$P < 0.05$, compared to ZX1, Holm-Bonferroni's post hoc). Dotted lines represent nonsignificant responses. (**F**) Representative transcranial FRISZ-TM fluorescence signals to broadband sounds before (black or cyan) and after (red or orange) ZX1 infusion in ZnT3 WT (top) or KO (bottom) mice. (**G**) Summary plot of average sound-evoked fluorescence signals from ZnT3 WT ($n = 4$) and KO ($n = 4$) mice. (ZnT3 WT: control versus ZX1: two-way ANOVA; effect of ZX1, $F = 16.02$, $P = 0.02$; *$P < 0.05$, compared to ZX1, Holm-Bonferroni's post hoc). Dotted lines represent nonsignificant responses. See table S1 for statistical details. Error bars indicate SEM.

among the most red-shifted FP-based indicators (Fig. 2A). A recent preprint described far-red fluorescent Ca^{2+} indicators based on cpFP, mKelly2 (*58*). Still, the excitation and emission of FRISZ are more red-shifted than these Ca^{2+} indicators by ~10 nm, allowing the effective excitation of FRISZ with common ~630-nm lasers or light-emitting diodes (LEDs). We thereby expect that the cpmMaroon scaffold of FRISZ may be adapted to expand the color palette of genetically encodable indicators for other analytical targets.

FRISZ displayed strong far-red fluorescence under both one-photon and two-photon excitation. For two-photon imaging, standard tunable Ti-sapphire lasers can excite FRISZ near 1060 nm to gain good brightness and Zn^{2+} responsiveness (Fig. 2, E and F). Moreover, because the fluorescence of FRISZ under 1200-nm excitation is relatively strong (*59*) and there is an emerging interest in using 1200-nm excitation to increase brain tissue transmittance (*60*), FRISZ may be a suitable indicator for these future experiments.

We successfully used FRISZ-TM to follow activity-dependent synaptic Zn^{2+} signals in acute brain slices in response to electrical stimuli. We observed that these signals were not completely abolished with the application of the extracellular Zn^{2+} chelator, ZX1 (Fig. 4D, red). Moreover, ZnT3 KO mice showed a small electrically evoked but stimulus intensity–independent increase in FRISZ-TM fluorescence, which was also not affected by ZX1 (Fig. 4F, cyan and orange). We attribute these nonspecific, ZX1- and ZnT3-independent signals to the weak responses of FRISZ to other cations (Fig. 2D) or the sensitivity of FRISZ to pH changes (fig. S5).

Moreover, we used FRISZ-TM to selectively detect sound intensity–dependent synaptic Zn^{2+} dynamics of A1 neurons in awake mice (Fig. 5). Sound-evoked FRISZ-TM signals in awake mice were also not completely abolished by ZX1 (Fig. 5D, red). However, in awake mice, unlike findings from the acute brain slices, ZnT3 KO mice showed no sound-evoked FRISZ-TM signals (Fig. 5F, cyan). Therefore, the residual ZX1-independent signals of FRISZ-TM in awake mice might be due to the inability of ZX1 to completely chelate extracellular Zn^{2+} in vivo. Together, we combined FRISZ-TM with ZnT3 KO mice and ZX1 pharmacology, confirming the dependence of the FRISZ-TM signals on synaptic (ZnT3-dependent) Zn^{2+} in response to electrical or sound stimulation (Figs. 4 and 5).

One limitation of FRISZ-TM is that it is genetically anchored to the extracellular cell membrane, including synaptic, extrasynaptic, and nonsynaptic regions, and thus, FRISZ-TM cannot discriminate whether Zn^{2+} signals are generated from synaptic or extra- and nonsynaptic areas. Consequently, FRISZ-TM may show reduced responses ($\Delta F/F_0$) to synaptic Zn^{2+} because the majority of FRISZ-TM may be expressed in extra- and nonsynaptic regions. As a result, FRISZ-TM might display relatively low activity-dependent changes in response to sound-evoked synaptic activity, thus underestimating synaptic Zn^{2+} signals.

Synaptic Zn^{2+} modulates NMDAR and AMPAR excitatory postsynaptic currents in response to a single presynaptic stimulus (*4*, *5*), and GABA type A receptor inhibitory postsynaptic currents in response to a single presynaptic action potential (*11*). However, consistent with previous studies using chemically synthesized fluorescent Zn^{2+} sensors (*4*, *5*, *61*), FRISZ-TM required trains of electrical stimuli to show Zn^{2+}-dependent fluorescence increases in brain slices. This is likely caused by the aforementioned nonoptimal localization issue: It is not yet possible to specifically localize the sensors in the synaptic cleft, where presynaptic release and postsynaptic transporters organize Zn^{2+} into distinct microdomains (*12*). To address these limitations, in our future studies, we plan to develop FRISZ variants that are selectively localized to synaptic sites, as progress has recently been made toward the localization of genetically encoded glutamate indicators at the synapses between neurons (*62*). Moreover, effort is ongoing to engineer next-generation FRISZ variants with faster Zn^{2+} association and dissociation kinetics, which will further enhance the ability to resolve synaptic Zn^{2+} pulses. In addition, we observed intracellular aggregations when the expression of FRISZ-TM was high, underestimating the overall $\Delta F/F_0$ because only the cell surface–displayed FRISZ could respond to extracellular synaptic Zn^{2+}. Toward this end, we plan to perform further studies to enhance the membrane localization robustness of this indicator. Last, future efforts will focus on two-photon imaging experiments on awake mice to track cell- and cell compartment–specific Zn^{2+} dynamics during audition.

Overall, we have developed a first-of-a-kind far-red-fluorescent cell-surface–anchored protein-based indicator for imaging synaptic Zn^{2+} in cortical brain slices in response to electrical activity and in awake mice in response to sound stimuli. Because synaptic Zn^{2+} is a potent neuromodulator throughout the cortex, our indicator is expected to improve the understanding of the roles of synaptic Zn^{2+} in cortical information processing beyond the A1 and even beyond sensory cortices (*3*, *16*, *63*). Moreover, in addition to the brain, FRISZ may be used to monitor the secretion of vesicular Zn^{2+} in other tissue types, such as pancreatic islets (*36*).

MATERIALS AND METHODS

Key materials and general methods

All chemicals were purchased from Thermo Fisher Scientific, Sigma-Aldrich, Thomas Scientific, and VWR. DNA oligos were purchased from Integrated DNA Technologies and Eurofins Genomics. Restriction enzymes were purchased from Thermo Fisher Scientific. DNA sequences were analyzed by Eurofins Genomics. Phusion High-Fidelity DNA polymerase from Thermo Fisher Scientific was used for DNA amplification and cloning. Taq DNA polymerase from New England Biolabs (in the presence of Mn^{2+}) and the GeneMorph II Random Mutagenesis Kit from Agilent were used for error-prone PCR. pcDNA3.1-mMaroon1 (Addgene, plasmid no. 83840) (*43*) was a gift from M. Lin (Stanford University). pCMV(MinDis).pCMV(MinDis)-iGluSnFR (Addgene, plasmid no. 41732) (*64*) was a gift from L. Looger (HHMI Janelia Research Campus). pAAV-hSyn-CheRiff-eGFP (Addgene, plasmid no. 51697) (*65*) was a gift from Adam Cohen (Harvard University). pTorPE-R-GECO1 (Addgene, plasmid no. 32465) (*66*) was a gift from R. Campbell (University of Alberta). pAdDeltaF6 (Addgene, plasmid no. 112867) and pAAV2/9n (Addgene, plasmid no. 112865) were gifts from J. M. Wilson (University of Pennsylvania). All animal procedures were conducted following the protocols approved by the Animal Care and Use Committees at the University of Virginia, University of Pittsburgh, and West Virginia University. C57BL/6J (the Jackson Laboratory, #000664), ZnT3 KO, and ZnT3 WT mice were used in this study. ZnT3 WT and ZnT3 KO littermates were generated by crossing heterozygous ZnT3 KO mice (the Jackson Laboratory, #005064) (*14*). Mice were hosted in temperature-controlled vivarium (~23°C) with a 12-hour/12-hour dark-light cycle and ~50% humidity.

Library construction and screening

The gene for the Rad50 zinc hook (AKGKCPVCGAELTD) was amplified from our previously reported ZIBG2 (*36*) and assembled via overlap extension PCRs with the fragments of the two cpmMaroon variants (cpmMaroon185-186 and cpmMaroon196-186) (*44*). The overlapped fragments were cloned into a modified pTorPE plasmid (*66*), which harbors a Twin-Strep-tag. Oligos with degenerate codons (NNK, where N = A, T, G, or C; and K = G or T) were used to randomize the links between the zinc hooks and cpmMaroon. In addition, error-prone PCRs were used for random mutagenesis of the whole gene fragment. Library screening was performed similarly to a previously described procedure (*66*). Briefly, digital fluorescence images of bacterial colonies were taken before and after spraying 2 mM EDTA (a Zn^{2+} chelator) via a fine mist sprayer. Colonies showing the extreme fluorescent ratio changes were selected and used to inoculate 1 ml of 2× Yeast Extract Tryptone (YT) medium supplemented with ampicillin (100 μg/ml) and 0.2% (w/v) L-arabinose in 96-well deep-well plates at 250 rpm and 16°C for 48 hours Cell lysates were then prepared from bacterial pellets using the Bacterial Protein Extraction Reagents. Fluorescence responses of the crude proteins to 100 μM Zn^{2+} or 100 μM EDTA were determined on a BioTek Synergy Mx microplate reader. Clones with large responses were chosen. Plasmids were prepared, sequenced, and used as templates in the further round of directed evolution.

Protein purification and characterization

FRISZ in pTorPE was cloned into a modified pBAD plasmid harboring a Twin-Strep-tag. The resultant plasmid was used to transform E. cloni 10G competent cells (Lucigen). Protein expression was performed as described (*44*). Cell pellets harvested by centrifugation were next lysed by sonication. The Twin-Strep–tagged protein was purified via affinity chromatography using a StrepTrap HP column (GE Healthcare). Next, the eluant was subjected to size exclusion chromatography through a HiLoad 16/600 Superdex 200 pg column (GE Healthcare). Purified proteins were buffer-exchanged and concentrated in a Hepes assay buffer [150 mM Hepes, 100 mM NaCl, 0.5 mM tris(2-carboxyethyl)phosphine (TCEP), and 10% glycerol (pH 7.4)] using Amicon Ultra Centrifugal Filter units (10,000-Da molecular weight cutoff). Freshly prepared proteins were next diluted with the Hepes assay buffer mentioned above for in vitro assays on a monochromator-based BioTek Synergy Mx plate reader. Solutions containing 200 nM protein and 100 μM Zn^{2+} or 100 μM EDTA in the Hepes assay buffer were prepared. The emission wavelength was set at 670 nm to record the excitation spectra, and the excitation light was scanned from 450 to 630 nm. The excitation wavelength was fixed at 590 nm to record the emission spectrum, and the emission was scanned from 610 to 800 nm. For other endpoint measurements, the excitation and emission were set at 610 and 650 nm, respectively. Zn^{2+} titrations were performed by mixing the protein (a final concentration of 100 nM) with a series of Hepes assay buffers supplemented with $ZnCl_2$ to provide free Zn^{2+} concentrations ranging from 100 nM to 1 mM. The fluorescent intensity of each solution was determined and plotted as a function of the Zn^{2+} concentration. The data were then fitted to the Hill equation. To determine the metal selectivity of the protein, various metals (a final concentration of 100 μM) were added to the Hepes assay buffer containing 500 nM protein. In particular, Cu^{+} was generated from Cu^{2+} in situ by mixing $CuCl_2$ (100 μM) and sodium ascorbate (500 μM), and the pH of the mixture was maintained at 7.4 by the Hepes assay buffer. The fluorescent intensity was recorded 10 min after mixing all components.

Determination of Zn^{2+} association and dissociation kinetics

A 10 mM Zn^{2+} stock was made by dissolving $ZnCl_2$ powder in HCl-acidified double-distilled H_2O (pH 2.5). A buffer containing 150 mM Hepes (pH 7.4), 100 mM NaCl, 0.5 mM TCEP, and 10% (v/v) glycerol was used to dilute Zn^{2+} and the purified FRISZ protein. The protein (75 μl) at the concentration of 100 nM was rapidly mixed with an equal volume of Zn^{2+} buffers at various concentrations (2, 20, 40, 60, and 80 μM) using an SFM 3000 stopped-flow mixing system (BioLogic). Fluorescence induced with 595-nm excitation was monitored using an MOS-200 optical system (BioLogic) equipped with a 610-nm long-pass (LP) filter (Edmund Optics). Data from 18 runs of each sample were used to obtain an average curve, and each experiment was further repeated with triplicate samples. The rate of appearance of the Zn^{2+}-bound protein state follows the rate law: $d[\text{FRISZ}{\cdot}Zn^{2+}]/dt = k_{on}\,[Zn^{2+}][\text{FRISZ}] - k_{off}\,[\text{FRISZ}]$. The experiments were designed such that $[Zn^{2+}] >> [\text{FRISZ}]$, so that $k_{on}\,[Zn^{2+}]$ remains constant throughout the experiments. In this case, the kinetics follow a pseudo first-order rate law and are described by the monoexponential function $\text{FRISZ}{\cdot}Zn^{2+}(t) = F_0 \exp(-k_{obs}t)$, where $k_{obs} = k_{on}\,[Zn^{2+}] + k_{off}$ (k_{on} and k_{off} are the rate constants for the association and dissociation of Zn^{2+} from the protein). A plot of the observed relaxation constant, k_{obs}, as a function of the Zn^{2+} concentration, therefore, yields a straight line, with a slope of k_{on} and a y intercept of k_{off}. The dissociation constant from the kinetic measurement ($K_{d,kinetic}$) is then obtained using the equation $K_{d,kinetic} = k_{off}/k_{on}$.

Determination of quantum yield, fluorescence lifetime, and extinction coefficients

For fluorescence measurements, the samples were diluted to have optical densities less than 0.09. Fluorescence quantum yields were determined using the absolute method with an integrating sphere instrument, Quantaurus-QY (Hamamatsu). In this measurement, the quantum yield (ϕ) was obtained at a set of excitation wavelengths changing from 500 and 590 nm with the step of 10 nm. For the Zn^{2+}-free (100 μM EDTA) and Zn^{2+}-saturated (100 μM Zn^{2+}) samples, quantum yield did not systematically change in the region from 520 (or 510) to 590 nm, so the average of the corresponding measurements was accepted as a final value. Fluorescence lifetimes were measured on dilute solutions with a Digital Frequency Domain system ChronosDFD (ISS) appended to a PC1 (ISS) photon counting spectrofluorometer. Fluorescence was excited with a 635-nm laser diode (ISS, model no. 73296) through a 640/10 filter. The excitation was modulated with multiple harmonics in the range of 10 to 300 MHz. LDS 798 dye (exciton) in ethanol with τ = 0.15 ns (*67*) was used as a lifetime standard to obtain the instrumental response function in each measurement. Fluorescence of the samples and standard were collected at 90° through HQ 705/100 and 695 LP filters to cutoff all excitation light. The modulation ratio and phase delay curves were fitted to model functions corresponding to a single- or double-exponential fluorescence decay with Vinci 3 software (ISS). Only double exponential decay functions provided acceptable χ^2 values, in the range of 0.59 to 0.73. The average fluorescence lifetime (calculated using intensity factors) is presented and used to calculate the extinction coefficient with the Strickler-Berg formula. Maximum extinction coefficients of the anionic forms (absorption at ~606 nm) of the chromophore (ε_A) were obtained using the Strickler-Berg formula that relates the extinction coefficient with fluorescence lifetime and quantum yield (*59*). To evaluate the extinction coefficient of the neutral form in both Zn^{2+}-free and Zn^{2+}-saturated states (absorption at 454 nm), we carried out a gradual alkaline titration of the samples and plotted the dependence of the neutral on anionic peak optical densities (*68*). The slope of this dependence is equal to the ratio of corresponding extinction coefficients. Neutral form extinction coefficient (ε_N) was then found from this ratio and a known extinction of anionic form. The fractional concentrations of the anionic (ρ_A) and neutral (ρ_N) forms can then be calculated using initial optical densities (at pH 7.4) of the two corresponding absorption peaks and their extinction coefficients from Beer′s law. Here, indexes A and N correspond to the anionic and neutral forms of the chromophore, respectively.

Two-photon spectral characterization

Two-photon excitation spectra were measured as described (*69*). In the spectral shape measurement, Coumarin 540A in dimethyl sulfoxide and LDS 798 in $CHCl_3$:$CDCl_3$ (1:2) were used as standards. A combination of 561 LP, 705/100, 770 short-pass (SP), and 694 SP filters was used to block both the laser scattering and spurious fluorescence peaking at 550 nm and corresponding to a species

absorbing near 530 nm. The cross section $\sigma_{2,A}$ was measured at two close wavelengths: 1060 and 1064 nm. The measurement was performed using rhodamine 6G in methanol at λ = 1060 nm (for which σ_2 = 10 ± 1 GM) (*69*) as a reference standard and, independently, using rhodamine B in alkaline ethanol at λ = 1064 nm (for which σ_2 = 13.3 ± 2.8 GM) (*58*) as an additional reference standard. The one- and two-photon excited fluorescence signals of the sample and reference solutions in the same collection conditions were measured, as described in (*58*). In these measurements, we used a combination of the 770 SP, 705/100, and 561 LP filters in the emission channel. Both reference standards gave very similar results for $\sigma_{2,A}$ either for Zn^{2+}-free or Zn^{2+}-saturated samples. To obtain the two-photon excitation spectrum in units of molecular brightness, we multiplied the $\sigma_{2,A}$ values measured at 1060 nm by independently measured ρ_A and ϕ_A (see the previous section), for FRISZ in Zn^{2+}-free and Zn^{2+}-saturated states and normalized the unscaled two-photon emission spectrum at 1060 nm to the product $F_2 = \rho_A \cdot \phi_A \cdot \sigma_{2,A}$ (1060). The molecular brightness of the anionic form presented in the Table 1 corresponds to the spectral maxima, λ_m, for both states of the sensor.

Construction of mammalian expression and viral packaging plasmids

The genetic fragment of FRISZ was amplified from the pTorPE plasmid and inserted into a predigested pCMV(MinDis)-iGluSnFR plasmid between the Bgl II and Sal I restriction sites, resulting in a plasmid termed pDisplay-FRISZ. To construct the AAV transfer plasmid, a genetic fragment encoding FRISZ, the N-terminal Igκ leading sequence, and the C-terminal PDGFRβ TM domain was amplified from pDisplay-FRISZ and inserted into a predigested pAAV-hSyn-CheRiff-eGFP plasmid between the BamH I and EcoR I restriction sites, resulting in a plasmid termed pAAV-hSyn-FRISZ-TM.

Culture, transfection, and imaging of HEK 293 T cells

HEK 293 T cells (American Type Culture Collection, #CRL-3216) were cultured and transfected as described (*36*). Fluorescence imaging was performed ~24 hours after transfection on a Leica DMi8 microscope equipped with a Leica SPE-II spectral confocal module and a Photometrics Prime 95B Scientific CMOS (complementary metal-oxide semiconductor) camera. Cells were washed three times with a modified Krebs-Ringer buffer [135 mM NaCl, 5 mM KCl, 0.4 mM K_2HPO_4, 1 mM $MgSO_4$, 1 mM $CaCl_2$, 5.5 mM glucose, and 20 mM Hepes (pH 7.4)] and imaged in this buffer using a 40× oil immersion objective lens. To determine cellular localization, the confocal module was used. The far-red fluorescence was acquired with a 635-nm laser, and the emission was collected at 655 to 800 nm. In addition to pDisplay-FRISZ, a cytosolic enhanced GFP (EGFP) (pcDNA3-EGFP) was expressed simultaneously for comparison. The green fluorescence was acquired with a 488-nm laser, and the emission was collected at 500 to 560 nm. To image the response of the indicator at the surface of HEK 293 T cells, time-lapse experiments were performed under the wide-field condition using the Photometrics Prime 95B Scientific CMOS camera and a Cy5 filter cube containing a 628/40 nm band-pass excitation filter and a 692/40 nm band-pass emission filter. Cells were imaged every 10 s for a 15-min duration. Confocal images were also acquired between each addition of the different stimulating chemicals. To determine the binding affinity of FRISZ at the surface of HEK 293 T cells, Zn^{2+} was added sequentially from low to high concentrations to gain 1 to 40 μM final concentrations, and cells were imaged every 1 min after thoroughly mixing the solution. To determine the half-time of the sensor for Zn^{2+} association and spontaneous dissociation, 200 μM Zn^{2+} was applied locally to the cells of interest, and time-lapse imaging with 15-ms exposure was performed. A glass micropipette with a ~4-μm-diameter tip was fabricated using a P-87 Flaming/Brown Micropipette Puller (Sutter), and a Picospritzer II microinjection dispenser was then used to deliver a buffered Zn^{2+} solution via the glass micropipette using a 3-ms puff. Photostability comparison was performed on an upright Scientifica SliceScope Pro 1000 equipped with a Photometrics Prime 95B Scientific CMOS camera and a CoolLed Enhanced pE-300^{white} LED light source. HEK 293 T cells expressing cell surface–localized FRISZ and mMaroon1 were continuously illuminated with excitation light set at 100%, which passed through a Cy5 filter set (Iridian, catalog no. FFS000008). Cells expressing cell surface–localized sfGFP were instead continuously illuminated with excitation light set at 29% through a GFP filter set (Iridian, catalog no. FFS000005). A digital optical power meter (Thorlabs, #PM100D) equipped with a microscope slide photodiode power sensor (Thorlabs, #S170C) was used to measure power at the focal plane. With the parameters mentioned above, both Cy5 and GFP channels had the same amount of power (4.677 mW). Using the field number of the objective lens provided by the manufacturer, the illumination area was next calculated from $\pi \cdot (0.5 \cdot D_{FOV})^2$, which was 0.3445 mm^2. Thus, the light intensity at the focal plane was calculated to be 1.35 W/cm^2.

Preparation of AAV

The AAV production was performed following a protocol from (*70*). The following plasmids (prepared from maxiprep) were used for AAV production: pAdDeltaF6, pAAV2/9n, and pAAV-hSyn-FRISZ-TM or pAAV-hSyn-mMaroon1-TM. Briefly, HEK 293 T cells cotransfected with the plasmids were incubated in high-glucose Dulbecco's modified Eagle's medium supplemented with 4% fetal bovine serum, 0.1 M sucrose, and 10 mM Hepes for 96 hours. Cells and medium were collected and separated via centrifugation. The supernatant medium was filtered through a 0.45-μm polyethersulfone membrane filter, and viral particles in the supernatant were further precipitated using a solution containing polyethylene glycol 8000 and NaCl. The viral particles were resuspended in a cell lysis buffer [50 mM tris, 150 mM NaCl, and 2 mM $MgCl_2$ (pH 8.5)]. The pelleted cells were resuspended in the cell lysis buffer mentioned above and lysed by sonication. The sonication mixture was clarified by centrifugation and combined with the crude viral particles harvested from the medium. After being treated with Benzonase nuclease (50 U/ml), the sample was cleared via centrifugation and then further purified via gradient ultracentrifugation. Last, the virus was collected and exchanged into Dulbecco's phosphate-buffered saline containing 0.001% pluronic and 200 mM NaCl. The viral solution was aliquoted, flash-frozen, and stored at −80°C. Viral titers were determined using a quantitative PCR method provided by Addgene. The typical viral titers were ~10^{14} genome copies/ml.

Stereotaxic injections for in vivo and ex vivo imaging

C57/B6J, ZnT3 WT, and ZnT3 KO mice between postnatal day 28 (P28) and P36 were injected with the AAVs into the right AC as

described previously (*48*, *49*). Briefly, mice were anesthetized with isoflurane, and a craniotomy (~0.4 mm in diameter) was made over the temporal cortex (~4 mm lateral to lambda). With a micromanipulator (Kopf), a glass micropipette containing the AAVs was inserted into the cortex of 0.5 to 0.7 mm past the surface of the dura, and ~ 500 nl of the virus was injected over 5 min. Next, the scalp of the mouse was closed with cyanoacrylate adhesive. Mice were given carprofen (5 mg/kg; Henry Schein Animal Health) to reduce the pain associated with the surgery and monitored for signs of postoperative stress and pain.

In vivo imaging preparation

About 21 to 28 days after the viral injections, mice were prepared for in vivo imaging as described previously (*48*, *49*). Briefly, mice were anesthetized and head-fixed, and a craniotomy (~1 mm in diameter) over the A1 (~4 mm lateral to lambda) was performed. To infuse the ZX1 into the AC, a micromanipulator (Siskiyou, Grants Pass, OR) was used to insert a glass micropipette backfilled with mineral oil and connected to a 5-μl glass syringe into the cortex at the edge of this craniotomy. The pipette contained artificial cerebrospinal fluid (ACSF) and 100 μM ZX1. Next, mice were placed under the microscope objective in a sound- and light-attenuation chamber containing a calibrated speaker (ES1, Tucker-Davis Davis Technologies, Alachua, FL).

In vivo wide-field imaging of the A1

After the in vivo imaging preparation, mice were unanesthetized to image the sound-evoked activity in the AC in awake mice, as described previously (*48*, *49*). The MATLAB-based Ephus program (*71*) was used to generate sound waveforms and synchronize the sound delivery and image acquisition hardware. We presented sound stimuli (6- to 64-kHz broadband noise, 100-ms duration, and 5-ms ramps at 30- to 80-dB SPL in 5-dB SPL increment level) while illuminating the skull with an orange LED (nominal wavelength of 590 nm; Thorlabs, M590L4). We imaged the change in FRISZ-TM or mMaroon1-TM emission with epifluorescence optics (Olympus U-MF2 filter cube: excitation filter FF01-593/40 nm, emission filter FF01-660/52 nm, and dichroic beam splitter FF635-Di01, AVR optics, Rochester, NY) and a 4× objective (Olympus) using a cooled charge-coupled device camera (Rolera, Q-Imaging, Surrey, BC, Canada). Images were acquired at a resolution of 174 × 130 pixels (4× spatial binning, each pixel covered an area of 171.1 μm^2) at a frame rate of 20 Hz in each mouse. An ROI (150 to 200 μm by 150 to 200 μm) over A1 was used to quantify sound-evoked responses. An average of the fluorescent intensity from all pixels in the ROI was derived. The sound-evoked change in fluorescence after the sound presentation (ΔF) was normalized to the baseline fluorescence (F_0), where F_0 is the average fluorescence of 1 s preceding the sound onset (for each pixel in the movie). $\Delta F/F_0$ responses from six to eight presentations of the same sound level were further averaged. Peak fluorescence signals during the 1-s period after the sound presentation were quantified as the sound-evoked response amplitude and were defined as significant responses if the sound-evoked changes ($\Delta F/F_0$) were 3 SD away from the baseline mean. After the initial recording, the ZX1 solution (100 μM) was infused into the AC at a rate of 30 nl/min over 20 min. Next, the pump speed was reduced to 9 nl/min, and the sound-evoked responses were remeasured.

Brain slice ex vivo imaging

Three to 4 weeks after the AAV injection, mice were transcardially perfused, and mouse brains were rapidly removed. Coronal slices (300 μm) containing the right AC were prepared in a cutting solution at 1°C using a vibratome (Leica, #VT1200 S) as described previously (*11*, *51*). The slices were immediately transferred and incubated at 34°C in a holding chamber for 40 min before imaging. The holding chamber contained ACSF containing the following: 125 mM NaCl, 2.5 mM KCl, 26.25 mM $NaHCO_3$, 2 mM $CaCl_2$, 1 mM $MgCl_2$, 10 mM glucose, 1.3 mM ascorbic acid, and 3 mM sodium pyruvate (pH 7.4; ~300 mOsm, bubbled with 95% O_2/5% CO_2). Next, ex vivo imaging was performed on brain slices bathed in carbonated ACSF identical to the incubating solution. The anatomical landmarks, such as the rhinal fissure and the underlying hippocampal formation, were used to locate the AC in brain slices. FRISZ-TM or mMaroon1-TM emission was imaged with epifluorescence optics as described above for in vivo wide-field imaging. Next, to image the stimulus-evoked change, L4 of AC was electrically stimulated with 0.3-ms-long 50-V pulses (1 to 100 pulses) at 100 Hz, starting at 3 s during each imaging session, by following a previous procedure (*5*). FRISZ-TM signals were imaged from L2/3 of AC. Each stimulus was presented six to eight times, and the average of each stimulus was taken for further analysis. To correct for gradual linear "run-down" in fluorescence signals with LED onset, a linear fit of the fluorescence signals from 2 s before the onset of the stimulus was subtracted from the stimulus and nonstimulus fluorescence signals. Next, fluorescence values were converted into $\Delta F/F_0$, with F_0 taken as the average baseline fluorescence from 1 s before the onset of the stimulus. Peak fluorescence signals during the 1-s period after the electrical stimulation were quantified as the stimulus-evoked response amplitude and were defined as significant responses if the electrical-evoked changes ($\Delta F/F_0$) were 3 SD higher than the baseline mean. After the initial recording, the ZX1 solution (100 μM) was bath applied to the brain slice over 20 min, and the stimulus-evoked change in FRISZ-TM fluorescence was remeasured.

Data analysis, statistics, and reproducibility

Microsoft Excel, MATLAB 2018a, GraphPad Prism, and Affinity Designer were used to analyze data and prepare figures for publication. Sample size and the number of replications for experiments are presented in figure legends. No statistical methods were used to predetermine the sample size. No data exclusions were performed. Blinding was not implemented, except for the ZnT3 WT versus KO experiments shown in Figs. 4 (F and G) and 5 (F and G) where the group identity was revealed after data collection and initial analysis. Cells and animals were randomly allocated to experimental groups. For comparisons between multiple groups having within-subject factors, a two-way repeated-measures analysis of variance (ANOVA) test was used. Bonferroni corrections were used for multiple two-sample post hoc comparisons among sample groups. The significance level ($\alpha = 0.05$) of the test was corrected via scaling by the reciprocal of the number of comparisons. Statistical details for Figs. 4 and 5 are presented in table S1. Data are shown as means and SD or SE (SEM), and the information is included in the figure legends. Fiji (ImageJ) was used to analyze microscopic images. The imaging background was typically subtracted by setting the rolling ball radius to 50 pixels. ROIs were manually drawn, and average intensities were extracted for further analysis.

When photobleaching was obvious, imaging stacks were corrected using a linear or exponential decay fitting of baselines.

Supplementary Materials

This PDF file includes:

Figs. S1 to S8
Table S1

REFERENCES AND NOTES

1. G. Danscher, G. Howell, J. Perez-Clausell, N. Hertel, The dithizone, Timm's sulphide silver and the selenium methods demonstrate a chelatable pool of zinc in CNS. A proton activation (PIXE) analysis of carbon tetrachloride extracts from rat brains and spinal cords intravitally treated with dithizone. *Histochemistry* **83**, 419–422 (1985).
2. C. E. Brown, R. H. Dyck, Distribution of zincergic neurons in the mouse forebrain. *J. Comp. Neurol.* **479**, 156–167 (2004).
3. R. F. Krall, T. Tzounopoulos, E. Aizenman, The function and regulation of Zinc in the brain. *Neuroscience* **457**, 235–258 (2021).
4. C. T. Anderson, R. J. Radford, M. L. Zastrow, D. Y. Zhang, U. P. Apfel, S. J. Lippard, T. Tzounopoulos, Modulation of extrasynaptic NMDA receptors by synaptic and tonic zinc. *Proc. Natl. Acad. Sci. U.S.A.* **112**, e2705–e2714 (2015).
5. B. I. Kalappa, C. T. Anderson, J. M. Goldberg, S. J. Lippard, T. Tzounopoulos, AMPA receptor inhibition by synaptically released zinc. *Proc. Natl. Acad. Sci. U.S.A.* **112**, 15749–15754 (2015).
6. B. I. Kalappa, T. Tzounopoulos, Context-dependent modulation of excitatory synaptic strength by synaptically released zinc. *eNeuro* **4**, e0011–17.2017 (2017).
7. T. Perez-Rosello, C. T. Anderson, F. J. Schopfer, Y. Zhao, D. Gilad, S. R. Salvatore, B. A. Freeman, M. Hershfinkel, E. Aizenman, T. Tzounopoulos, Synaptic Zn^{2+} inhibits neurotransmitter release by promoting endocannabinoid synthesis. *J. Neurosci.* **33**, 9259–9272 (2013).
8. P. Paoletti, P. Ascher, J. Neyton, High-affinity zinc inhibition of NMDA NR1-NR2A receptors. *J. Neurosci.* **17**, 5711–5725 (1997).
9. A. M. Vergnano, N. Rebola, L. P. Savtchenko, P. S. Pinheiro, M. Casado, B. L. Kieffer, D. A. Rusakov, C. Mulle, P. Paoletti, Zinc dynamics and action at excitatory synapses. *Neuron* **82**, 1101–1114 (2014).
10. A. Morabito, Y. Zerlaut, B. Serraz, R. Sala, P. Paoletti, N. Rebola, Activity-dependent modulation of NMDA receptors by endogenous zinc shapes dendritic function in cortical neurons. *Cell Rep.* **38**, 110415 (2022).
11. S. Kouvaros, M. Kumar, T. Tzounopoulos, Synaptic zinc enhances inhibition mediated by somatostatin, but not parvalbumin, cells in mouse auditory cortex. *Cereb. Cortex* **30**, 3895–3909 (2020).
12. R. F. Krall, A. Moutal, M. B. Phillips, H. Asraf, J. W. Johnson, R. Khanna, M. Hershfinkel, E. Aizenman, T. Tzounopoulos, Synaptic zinc inhibition of NMDA receptors depends on the association of GluN2A with the zinc transporter ZnT1. *Sci. Adv.* **6**, eabb1515 (2020).
13. N. Upmanyu, J. Jin, H. von der Emde, M. Ganzella, L. Bösche, V. N. Malviya, E. Zhuleku, A. Politi, M. Ninov, I. Silbern, M. Leutenegger, H. Urlaub, D. Riedel, J. Preobraschenski, I. Milosevic, S. W. Hell, R. Jahn, S. Sambandan, Colocalization of different neurotransmitter transporters on synaptic vesicles is sparse except for VGLUT1 and ZnT3. *Neuron* **110**, 1483–1497.e7 (2022).
14. T. B. Cole, H. J. Wenzel, K. E. Kafer, P. A. Schwartzkroin, R. D. Palmiter, Elimination of zinc from synaptic vesicles in the intact mouse brain by disruption of the ZnT3 gene. *Proc. Natl. Acad. Sci. U.S.A.* **96**, 1716–1721 (1999).
15. L. J. Blakemore, P. Q. Trombley, Zinc modulates olfactory bulb kainate receptors. *Neuroscience* **428**, 252–268 (2020).
16. B. B. McAllister, R. H. Dyck, Zinc transporter 3 (ZnT3) and vesicular zinc in central nervous system function. *Neurosci. Biobehav. Rev.* **80**, 329–350 (2017).
17. J. H. Weiss, S. L. Sensi, Ca^{2+}-Zn^{2+} permeable AMPA or kainate receptors: Possible key factors in selective neurodegeneration. *Trends Neurosci.* **23**, 365–371 (2000).
18. A. Birinyi, D. Parker, M. Antal, O. Shupliakov, Zinc co-localizes with GABA and glycine in synapses in the lamprey spinal cord. *J. Comp. Neurol.* **433**, 208–221 (2001).
19. Z. Wang, J. Y. Li, A. Dahlstrom, G. Danscher, Zinc-enriched GABAergic terminals in mouse spinal cord. *Brain Res.* **921**, 165–172 (2001).
20. A. Paul, M. Crow, R. Raudales, M. He, J. Gillis, Z. J. Huang, Transcriptional architecture of synaptic communication delineates GABAergic neuron identity. *Cell* **171**, 522–539.e20 (2017).
21. K. Hirzel, U. Müller, A. T. Latal, S. Hülsmann, J. Grudzinska, M. W. Seeliger, H. Betz, B. Laube, Hyperekplexia phenotype of glycine receptor α1 subunit mutant mice identifies Zn^{2+} as an essential endogenous modulator of glycinergic neurotransmission. *Neuron* **52**, 679–690 (2006).
22. T. Perez-Rosello, C. T. Anderson, C. Ling, S. J. Lippard, T. Tzounopoulos, Tonic zinc inhibits spontaneous firing in dorsal cochlear nucleus principal neurons by enhancing glycinergic neurotransmission. *Neurobiol. Dis.* **81**, 14–19 (2015).
23. S. L. Sensi, H. Z. Yin, J. H. Weiss, Glutamate triggers preferential Zn^{2+} flux through Ca^{2+} permeable AMPA channels and consequent ROS production. *Neuroreport* **10**, 1723–1727 (1999).
24. P. A. Adlard, J. M. Parncutt, D. I. Finkelstein, A. I. Bush, Cognitive loss in zinc transporter-3 knock-out mice: A phenocopy for the synaptic and memory deficits of Alzheimer's disease? *J. Neurosci.* **30**, 1631–1636 (2010).
25. C. J. Frederickson, J. Y. Koh, A. I. Bush, The neurobiology of zinc in health and disease. *Nat. Rev. Neurosci.* **6**, 449–462 (2005).
26. V. Kumar, A. Kumar, K. Singh, K. Avasthi, J. J. Kim, Neurobiology of zinc and its role in neurogenesis. *Eur. J. Nutr.* **60**, 55–64 (2021).
27. T. W. Chen, T. J. Wardill, Y. Sun, S. R. Pulver, S. L. Renninger, A. Baohan, E. R. Schreiter, R. A. Kerr, M. B. Orger, V. Jayaraman, L. L. Looger, K. Svoboda, D. S. Kim, Ultrasensitive fluorescent proteins for imaging neuronal activity. *Nature* **499**, 295–300 (2013).
28. E. Pan, X. A. Zhang, Z. Huang, A. Krezel, M. Zhao, C. E. Tinberg, S. J. Lippard, J. O. McNamara, Vesicular zinc promotes presynaptic and inhibits postsynaptic long-term potentiation of mossy fiber-CA3 synapse. *Neuron* **71**, 1116–1126 (2011).
29. K. M. Dean, Y. Qin, A. E. Palmer, Visualizing metal ions in cells: An overview of analytical techniques, approaches, and probes. *Biochim. Biophys. Acta* **1823**, 1406–1415 (2012).
30. K. P. Carter, A. M. Young, A. E. Palmer, Fluorescent sensors for measuring metal ions in living systems. *Chem. Rev.* **114**, 4564–4601 (2014).
31. E. P. S. Pratt, L. J. Damon, K. J. Anson, A. E. Palmer, Tools and techniques for illuminating the cell biology of zinc. *Biochim. Biophys. Acta Mol. Cell Res.* **1868**, 118865 (2021).
32. A. M. Hessels, M. Merkx, Genetically-encoded FRET-based sensors for monitoring Zn^{2+} in living cells. *Metallomics* **7**, 258–266 (2015).
33. Y. Nasu, Y. Shen, L. Kramer, R. E. Campbell, Structure- and mechanism-guided design of single fluorescent protein-based biosensors. *Nat. Chem. Biol.* **17**, 509–518 (2021).
34. J. L. Vinkenborg, T. J. Nicolson, E. A. Bellomo, M. S. Koay, G. A. Rutter, M. Merkx, Genetically encoded FRET sensors to monitor intracellular Zn^{2+} homeostasis. *Nat. Methods* **6**, 737–740 (2009).
35. P. J. Dittmer, J. G. Miranda, J. A. Gorski, A. E. Palmer, Genetically encoded sensors to elucidate spatial distribution of cellular zinc. *J. Biol. Chem.* **284**, 16289–16297 (2009).
36. M. Chen, S. Zhang, Y. Xing, X. Li, Y. He, Y. Wang, J. Oberholzer, H. W. Ai, Genetically encoded, photostable indicators to image dynamic Zn^{2+} secretion of pancreatic islets. *Anal. Chem.* **91**, 12212–12219 (2019).
37. Z. Chen, H. W. Ai, Single fluorescent protein-based indicators for zinc ion (Zn^{2+}). *Anal. Chem.* **88**, 9029–9036 (2016).
38. Y. Qin, D. W. Sammond, E. Braselmann, M. C. Carpenter, A. E. Palmer, Development of an optical Zn^{2+} probe based on a single fluorescent protein. *ACS Chem. Biol.* **11**, 2744–2751 (2016).
39. D. H. Fudge, R. Black, L. Son, K. LeJeune, Y. Qin, Optical recording of Zn^{2+} dynamics in the mitochondrial matrix and intermembrane space with the GZnP2 sensor. *ACS Chem. Biol.* **13**, 1897–1905 (2018).
40. A. M. Grabrucker, M. Rowan, C. C. Garner, Brain-delivery of zinc-ions as potential treatment for neurological diseases: Mini review. *Drug Deliv. Lett.* **1**, 13–23 (2011).
41. J. N. Henderson, H. W. Ai, R. E. Campbell, S. J. Remington, Structural basis for reversible photobleaching of a green fluorescent protein homologue. *Proc. Natl. Acad. Sci. U.S.A.* **104**, 6672–6677 (2007).
42. K. P. Hopfner, L. Craig, G. Moncalian, R. A. Zinkel, T. Usui, B. A. Owen, A. Karcher, B. Henderson, J. L. Bodmer, C. T. McMurray, J. P. Carney, J. H. Petrini, J. A. Tainer, The Rad50 zinc-hook is a structure joining Mre11 complexes in DNA recombination and repair. *Nature* **418**, 562–566 (2002).
43. B. T. Bajar, A. J. Lam, R. K. Badiee, Y. H. Oh, J. Chu, X. X. Zhou, N. Kim, B. B. Kim, M. Chung, A. L. Yablonovitch, B. F. Cruz, K. Kulalert, J. J. Tao, T. Meyer, X. D. Su, M. Z. Lin, Fluorescent indicators for simultaneous reporting of all four cell cycle phases. *Nat. Methods* **13**, 993–996 (2016).
44. T. Wu, Y. Pang, H. W. Ai, Circularly permuted far-red fluorescent proteins. *Biosensors* **11**, 438 (2021).
45. Y. Hori, K. Suzuki, Y. Okuno, M. Nagaoka, S. Futaki, Y. Sugiura, Artificial Zinc finger peptide containing a novel His4 domain. *J. Am. Chem. Soc.* **122**, 7648–7653 (2000).
46. S. J. Strickler, R. A. Berg, Relationship between absorption intensity and fluorescence lifetime of molecules. *J. Chem. Phys.* **37**, 814–822 (1962).
47. J. D. Pedelacq, S. Cabantous, T. Tran, T. C. Terwilliger, G. S. Waldo, Engineering and characterization of a superfolder green fluorescent protein. *Nat. Biotechnol.* **24**, 79–88 (2006).

48. C. T. Anderson, M. Kumar, S. Xiong, T. Tzounopoulos, Cell-specific gain modulation by synaptically released zinc in cortical circuits of audition. *eLife* **6**, e29893 (2017).
49. M. Kumar, S. Xiong, T. Tzounopoulos, C. T. Anderson, Fine control of sound frequency tuning and frequency discrimination acuity by synaptic zinc signaling in mouse auditory cortex. *J. Neurosci.* **39**, 854–865 (2019).
50. P. A. Cody, T. Tzounopoulos, Neuromodulatory mechanisms underlying contrast gain control in mouse auditory cortex. *J. Neurosci.* **42**, 5564–5579 (2022).
51. A. Joshi, J. W. Middleton, C. T. Anderson, K. Borges, B. A. Suter, G. M. Shepherd, T. Tzounopoulos, Cell-specific activity-dependent fractionation of layer 2/3→5B excitatory signaling in mouse auditory cortex. *J. Neurosci.* **35**, 3112–3123 (2015).
52. S. Gautam, A. Perron, H. Mutoh, T. Knopfel, Exploration of fluorescent protein voltage probes based on circularly permuted fluorescent proteins. *Front. Neuroeng.* **2**, 14 (2009).
53. S. A. Filatova, I. A. Shcherbakov, V. B. Tsvetkov, Optical properties of animal tissues in the wavelength range from 350 to 2600 nm. *J. Biomed. Opt.* **22**, 35009 (2017).
54. Y. Qian, K. D. Piatkevich, B. Mc Larney, A. S. Abdelfattah, S. Mehta, M. H. Murdock, S. Gottschalk, R. S. Molina, W. Zhang, Y. Chen, J. Wu, M. Drobizhev, T. E. Hughes, J. Zhang, E. R. Schreiter, S. Shoham, D. Razansky, E. S. Boyden, R. E. Campbell, A genetically encoded near-infrared fluorescent calcium ion indicator. *Nat. Methods* **16**, 171–174 (2019).
55. Y. Qian, D. M. O. Cosio, K. D. Piatkevich, S. Aufmkolk, W. C. Su, O. T. Celiker, A. Schohl, M. H. Murdock, A. Aggarwal, Y. F. Chang, P. W. Wiseman, E. S. Ruthazer, E. S. Boyden, R. E. Campbell, Improved genetically encoded near-infrared fluorescent calcium ion indicators for in vivo imaging. *PLOS Biol.* **18**, e3000965 (2020).
56. T. W. Sedlak, M. Saleh, D. S. Higginson, B. D. Paul, K. R. Juluri, S. H. Snyder, Bilirubin and glutathione have complementary antioxidant and cytoprotective roles. *Proc. Natl. Acad. Sci. U.S.A.* **106**, 5171–5176 (2009).
57. F. Montecinos-Franjola, J. Y. Lin, E. A. Rodriguez, Fluorescent proteins for in vivo imaging, where's the biliverdin? *Biochem. Soc. Trans.* **48**, 2657–2667 (2020).
58. R. Dalangin, M. Drobizhev, R. S. Molina, A. Aggarwal, R. Patel, A. S. Abdelfattah, Y. Zhao, J. Wu, K. Podgorski, E. R. Schreiter, T. E. Hughes, R. E. Campbell, Y. Shen, Far-red fluorescent genetically encoded calcium ion indicators. bioRxiv 2020.11.12.380089 [Preprint]. 15 November 2020. https://doi.org/10.1101/2020.11.12.380089.
59. M. Drobizhev, N. S. Makarov, S. E. Tillo, T. E. Hughes, A. Rebane, Two-photon absorption properties of fluorescent proteins. *Nat. Methods* **8**, 393–399 (2011).
60. M. Wang, C. Wu, D. Sinefeld, B. Li, F. Xia, C. Xu, Comparing the effective attenuation lengths for long wavelength in vivo imaging of the mouse brain. *Biomed. Opt. Express* **9**, 3534–3543 (2018).
61. J. Qian, J. L. Noebels, Visualization of transmitter release with zinc fluorescence detection at the mouse hippocampal mossy fibre synapse. *J. Physiol.* **566**, 747–758 (2005).
62. Y. Shindo, K. Ashida, K. Masamoto, H. Takuwa, M. Takahashi, M. Higuchi, R. Ide, K. Hotta, K. Oka, Genetically encoded sensors for analysing neurotransmission among synaptically-connected neurons. bioRxiv 2022.04.03.486903 [Preprint]. 5 April 2022. https://doi.org/10.1101/2022.04.03.486903.
63. B. B. McAllister, R. H. Dyck, A new role for zinc in the brain. *eLife* **6**, e31816 (2017).
64. J. S. Marvin, B. G. Borghuis, L. Tian, J. Cichon, M. T. Harnett, J. Akerboom, A. Gordus, S. L. Renninger, T. W. Chen, C. I. Bargmann, M. B. Orger, E. R. Schreiter, J. B. Demb, W. B. Gan, S. A. Hires, L. L. Looger, An optimized fluorescent probe for visualizing glutamate neurotransmission. *Nat. Methods* **10**, 162–170 (2013).
65. D. R. Hochbaum, Y. Zhao, S. L. Farhi, N. Klapoetke, C. A. Werley, V. Kapoor, P. Zou, J. M. Kralj, D. Maclaurin, N. Smedemark-Margulies, J. L. Saulnier, G. L. Boulting, C. Straub, Y. K. Cho, M. Melkonian, G. K. S. Wong, D. J. Harrison, V. N. Murthy, B. L. Sabatini, E. S. Boyden, R. E. Campbell, A. E. Cohen, All-optical electrophysiology in mammalian neurons using engineered microbial rhodopsins. *Nat. Methods* **11**, 825–833 (2014).
66. Y. Zhao, S. Araki, J. Wu, T. Teramoto, Y. F. Chang, M. Nakano, A. S. Abdelfattah, M. Fujiwara, T. Ishihara, T. Nagai, R. E. Campbell, An expanded palette of genetically encoded Ca^{2+} indicators. *Science* **333**, 1888–1891 (2011).
67. R. Luchowski, Z. Gryczynski, P. Sarkar, J. Borejdo, M. Szabelski, P. Kapusta, I. Gryczynski, Instrument response standard in time-resolved fluorescence. *Rev. Sci. Instrum.* **80**, 033109 (2009).
68. L. M. Barnett, T. E. Hughes, M. Drobizhev, Deciphering the molecular mechanism responsible for GCaMP6m's Ca^{2+}-dependent change in fluorescence. *PLoS ONE* **12**, e0170934 (2017).
69. M. Drobizhev, R. S. Molina, T. E. Hughes, Characterizing the two-photon absorption properties of fluorescent molecules in the 680-1300 nm spectral range. *Bio Protoc.* **10**, e3498 (2020).
70. M. Rego, L. M. Hanley, I. Ersing, K. Guerin, M. Tasissa, L. Haery, I. Mueller, E. Sanders, M. Fan, Improved yield of AAV2 and rAAV2-retro serotypes following sugar supplementation during the viral production phase. bioRxiv 488585 [**Preprint**]. 10 December 2018. https://doi.org/10.1101/488585.
71. B. A. Suter, T. O'Connor, V. Iyer, L. T. Petreanu, B. M. Hooks, T. Kiritani, K. Svoboda, G. M. Shepherd, Ephus: Multipurpose data acquisition software for neuroscience experiments. *Front. Neural Circuits* **4**, 100 (2010).

Acknowledgments: We thank X. Li and Z. Li for technical assistance and replicating some results. **Funding:** Research reported in this publication was supported by funding to H.-w.A. (University of Virginia Start-up Package and NIH grants R01 EB033172, R01 DK122253, RF1 AG077773, and R01 GM129291), T.T. (NSF-IOS-1655480 and NIH grants R01 EB033172, R01 DC019618, and R01 DC007905), M.K. (Hearing Health Foundation award 855358), M.D. (NIH BRAIN grant U24 NS109107), C.T.A. (The Whitehall Foundation grant 2020-05-44 and NIH grant R35 GM138023), and M.M. (NIH grant T32 GM132494). **Author contributions:** H.-w.A., T.T., and M.K. conceived this collaborative project. T.W. engineered the indicator and performed the characterization in vitro and cultured cells, viral preparation, and initial tests in mice with contributions from J.Z., S.Z., X.T., and Y.Z. M.D. determined most photophysical parameters and performed in vitro two-photon characterization. Y.W. and A.A. performed the stopped-flow experiment. M.K., T.T., M.M., and C.T.A. designed in vivo and ex vivo imaging experiments. M.K. performed in vivo wide-field and ex vivo brain-slice imaging. T.W., J.Z., M.D., A.A., M.K., and M.M. analyzed data. H.-w.A., T.W., M.K., M.D., C.T.A., and T.T. wrote the manuscript. **Competing interests:** The authors declare that they have no competing interests. **Data and materials availability:** The plasmids for pTorPE-FRISZ (plasmid no. 176888), pDisplay-FRISZ (plasmid no. 176887), pAAV-hSyn-FRISZ-TM (plasmid no. 176886), and their sequence information have been deposited to Addgene. All data needed to evaluate the conclusions in the paper are present in the paper and/or the Supplementary Materials.

Submitted 26 May 2022
Accepted 1 February 2023
Published 1 March 2023
10.1126/sciadv.add2058